Effects of the Hunga Tonga-Hunga Ha'apai Eruption on MODIS-retrieved Sea Surface Temperatures

Chong Jia[1] and Peter J. Minnett[2]

[1]Graduate Program of Meteorology and Physical Oceanography, Rosenstiel School of Marine, Atmospheric, and Earth Science, University of Miami, Miami, FL, USA.

[2]Department of Ocean Sciences, Rosenstiel School of Marine, Atmospheric, and Earth Science, University of Miami, Miami, FL, USA.

Corresponding author: Chong Jia (chong.jia@earth.miami.edu)

Key Points:

- Stratospheric sulfate aerosols in Tonga eruption plume affect sea-surface temperature from Moderate Resolution Imaging Spectroradiometer.
- Negative biases of sea-surface temperature were pronounced in Southern Hemispheric tropics initially and spread to mid-latitude after May.
- A negative offset of 11-12 μm brightness temperature difference is due to more absorption by aerosol at 11 μm, opposite to H_2O absorption.

Abstract

The eruption of Hunga Tonga-Hunga Ha'apai (HTHH) volcano on 15 January 2022 injected a great amount of H_2O and a moderate amount of SO_2 into the stratosphere, producing a pronounced and persistent sulfate aerosol layer centered around the mid-stratosphere, mostly confined to Southern Hemisphere (SH) tropics. These aerosols affect the Moderate Resolution Imaging Spectroradiometer (MODIS) retrievals of sea surface temperature (SST) where negative biases reached -0.3 K and an annual mean of -0.1 K north of 40ºS in the SH. The spatial and temporal evolutions of MODIS SST anomalies are presented. Radiative transfer simulations demonstrate the aerosol effect on MODIS SST retrievals by causing an additional brightness temperature (BT) deficit at 11 μm and a reduction in BT differences since the characteristic of spectral attenuation between 11 μm and 12 μm is opposite to that of H_2O. A correction for HTHH aerosol effects in the retrieval algorithm is therefore desirable.

Plain Language Summary

A submarine volcano, Hunga Tonga-Hunga Ha'apai, erupted on 15 January 2022 injecting gases and aerosols into the stratosphere. Subsequently, the sea surface temperature (SST) derived from the Moderate Resolution Imaging Spectroradiometer (MODIS) onboard the Aqua satellite is found to be lower than expected when compared to the in situ SST measured by drifting buoys at mid-low latitudes in the Southern Hemisphere. The negative biases are shown to be more associated with the anomalies in stratospheric sulfate aerosol than in water vapor, and persisted at least until the end of 2022. The model simulated aerosol-induced SST errors are comparable to those measured, further verifying the aerosol effect on MODIS-derived SST. It is important to generate a correction strategy due to high accuracy requirements for SST in scientific studies, e.g., as the input to climate models.

1 Introduction

Infrared (IR) radiometers onboard satellites provide global coverage and frequent skin sea surface temperature (SST) retrievals, such as Moderate Resolution Imaging Spectroradiometer (MODIS; [*Kilpatrick et al.*, 2015]) and the Visible Infrared Imaging Radiometer Suite (VIIRS; [*Minnett et al.*, 2020]). The current retrieval algorithms for both MODIS and VIIRS, using the channels centered at 11 μm and 12 μm, the longwave IR atmospheric "window", are applicable for daytime and nighttime measurements and are a modification of the nonlinear SST algorithm (NLSST) of *Walton et al.* [1998] with the following form:

$$SST_{sat} = a_0 + a_1 BT_{11} + a_2 (BT_{11} - BT_{12}) T_{sfc} + a_3 (\sec\theta - 1)(BT_{11} - BT_{12}) + a_4 (mirror) + a_5 (\theta) + a_6 (\theta^2) \quad (1)$$

where BT_{11} and BT_{12} are brightness temperatures (BTs) in the 11 μm and 12 μm channels. T_{sfc} is a reference SST. θ is the sensor zenith angle. Coefficients a_0-a_6 are derived by regression of matchups between the in situ and satellite measurements, monthly with latitude-band dependence. The algorithm is described in detail by *Kilpatrick et al.* [2015] and *Jia and Minnett* [2020].

The NLSST algorithm mainly accounts for the atmospheric attenuation effects of water vapor (H_2O); but satellite retrievals are highly affected in aerosol-contaminated regions, for example caused by the tropospheric dust from the Saudi Arabian and Sahara deserts. *Luo et al.* [2019] demonstrated the aerosol effect on MODIS retrieved SST and introduced an improved algorithm for nighttime data in the Saharan dust outflow area. Nevertheless, beyond dust aerosol, dramatic volcanic explosions inject large amounts of aerosol into the stratosphere, such as Mt. Pinatubo (Philippines, 1991) and El Chichón (Mexico, 1982), the two largest volcanic eruptions in the 20th century. *Reynolds et al.* [1989] showed a mean bias of -0.3 K for the Advanced Very High Resolution Radiometer (AVHRR) multichannel SST from 1982 to 1984 associated with the stratospheric aerosol due to El Chichón eruptions. *Reynolds* [1993] further studied the impact of Mt. Pinatubo aerosols on AVHRR SST, where nighttime data had average negative biases with magnitudes > 1 K between 20ºN and 20ºS in August and September 1991 even though using an aerosol-corrected equation.

The submarine eruption of volcano Hunga Tonga-Hunga Ha'apai (HTHH) (20.54°S, 175.38°W) on 15 January 2022 was the most explosive eruption since Mt. Pinatubo in 1991, with a volcanic explosivity index of 5 [*Jenkins et al.*, 2023]. Differing from the terrestrial volcanos mentioned above, HTHH injected an unprecedented mass of H_2O into the stratosphere, up to 146 Tg [*Millán et al.*, 2022] ~10% of the total stratospheric burden. In contrast, the sulfur dioxide (SO_2) injection was surprisingly low, estimated ~0.4 Tg from several satellite instruments [*Carn et al.*, 2022; *Millán et al.*, 2022], whereas Mt. Pinatubo lofted ~20 Tg SO_2 into the stratosphere [*Guo et al.*, 2004; *Read et al.*, 1993]. However, it was the greatest perturbation of stratospheric aerosols since the Mt. Pinatubo eruption with 1~3 Tg of sulfate aerosol injected [*Sellitto et al.*, 2022], due to the enhancement of H_2O resulting in shorter SO_2 lifetimes and faster sulfate particle coagulation [*Zhu et al.*, 2022]. Despite the relatively small amount of SO_2 put into the stratosphere, we will show that it is the sulfate aerosols are the main culprit in reducing the SST retrieval accuracy.

This paper focuses on the SST dataset derived from MODIS on Aqua and uses auxiliary aerosol measurements from various spaceborne sensors to study the characteristics of potential SST biases related to the stratospheric aerosol anomaly. Section 2 gives a brief description of the instruments and datasets. Section 3 describes the fundamental pattern of MODIS SST bias dependence on HTHH sulfate aerosols, as well as its evolution. Radiative transfer simulations were used to quantitively validate such stratospheric aerosol impacts. Section 4 presents the summary and discussion.

2 Data

To assess the accuracy of MODIS retrieved SST, a matchup database (MUDB) has been established by collocating satellite-derived SST, BTs derived from radiance measurements, in situ drifting buoy SST (SST_{buoy}) and other ancillary information (e.g., time, location, quality level (QL) flag and viewing geometry). The time window between satellite and field measurements is < 30 min, and the distance is < 10 km [*Kilpatrick et al.*, 2015]. Here, the good quality data with QL = 0 (best) and QL = 1 (degraded, generally by long atmospheric path lengths) are used, and the SST bias, ΔSST, is defined as:

$$\Delta SST = SST_{sat} - SST_{buoy} \quad (2)$$

For the aerosol products, MODIS aerosol optical depth (AOD) at a wavelength of 550 nm is firstly taken from the MYD04_L2 files, applying the Dark Target algorithm over the ocean [*Levy et al.*, 2013; *Remer et al.*, 2005]. Those granule-level data are produced at a horizontal pixel size (at nadir) of 10 km × 10 km.

The Rutherford Appleton Laboratory Infrared/Microwave Sounder (IMS) retrieval core scheme [*Siddans*, 2019] retrieves sulfate-specific optical depth (SOD) at 1170 cm^{-1}, the peak of the mid-infrared extinction cross section [*Sellitto and Legras*, 2016], using the Radiative Transfer for TOVS (RTTOV) v12 [*Saunders et al.*, 2017]. The IMS SOD data are gridded on 0.25º (latitude) × 0.25º (longitude) and provided as two sets of daily files from the daytime and nighttime parts of the orbits separately.

The Ozone Mapping and Profiler Suite Limb Profiler (OMPS-LP) onboard the Suomi-NPP satellite provides relatively high-resolution vertical aerosol profiles and integrated stratospheric AOD (sAOD) in six visible bands. We use v2.1 algorithm with a newly added variable, the aerosol to molecular extinction ratio (AMER), analogous to aerosol mixing ratio, and the retrievals at 997 nm as recommended by *Taha et al.* [2021], discarding swaths with non-zero quality flag. The OMPS-LP data are projected and averaged daily onto a 1º × 2º latitude-longitude grid.

The Microwave Limb Sounder (MLS) on board NASA's Aura satellite provides H_2O mixing ratio derived from radiances measured primarily by the 190 GHz radiometer [*Livesey et al.*, 2006]. We use v4 without quality screening as validated by *Millán et al.* [2022]. The MLS data are projected and averaged daily onto a 2º × 4º latitude-longitude grid.

Surface and vertical profiles of meteorological data are taken from MERRA-2 reanalysis [*Gelaro et al.*, 2017], including temperature, specific humidity and wind speed.

3 Results

3.1 General Effect of the HTHH Eruption on MODIS SST

The study region is from 40ºS to 0º and from 180ºW to 180ºE. Table 1 shows the MODIS SSTs in 2022 generally have an additional ~0.1 K negative bias and ~26% reduction in the number of matchups compared with 2021, which occur not only throughout the day but also in both QL0 and QL1 data. The negative biases are more pronounced in QL1 retrievals due to their longer path lengths. Those anomalies are associated with the HTHH eruption. Note that MODIS-derived SSTs are anticipated to be cooler than in situ buoy measurements by ~0.17 K on average [*Donlon et al.*, 2002; *Minnett et al.*, 2016] due to the cool skin layer effect. Figure 1a-b presents the spatial distribution of ΔSST in 2021 and 2022. Firstly, the number of matchups is much smaller in the equatorial regions than elsewhere because of the surface flow divergence leading to buoys drifting toward the central ocean gyres [*Lumpkin et al.*, 2012]. Furthermore, the increased negative biases in the retrieved SST in 2022 are distributed in the whole zonal area, so are the drops of data volume (Table S1 in Supporting Information S1). In the region centered around the location of volcanic eruption (30°S -10°S, 150°E-150°W), the mean ΔSST reaches -0.53 K with a reduction in the number of matchups up to 36%. Figure 1c further demonstrates the more frequent negative ΔSSTs after the HTHH eruption, but the shape of the distribution is barely changed with a cold tail, usually explained as resulting from undetected cloud contamination or effects of extreme atmospheric conditions [*Szczodrak et al.*, 2014]. Therefore, such a negative offset of ΔSST indicates an under-compensation in the NLSST atmospheric correction algorithm following the eruption.

Having included the MODIS AOD retrievals at 550 nm in the MUDB, Figure 1d shows the ΔSST has a significantly negative relationship with AOD. From the statistics of ΔSST (Table S2 in Supporting Information S1), when the AOD < 0.1, the MODIS SSTs are scarcely affected by aerosols. The aerosol effect becomes more pronounced with increasing AOD, illustrating its influence on errors in SST retrievals. Figure 1e demonstrates the larger fraction of AOD > 0.1 in 2022, which strongly verifies the hypothesis of aerosol contamination due to the HTHH eruption. Note that the regression slopes for 2021 and 2022 data are not significantly different at the 95% confidence level based on the t-statistic test. This is likely a consequence of the cloud screening algorithm used in the R2019 MODIS SST retrievals [*Kilpatrick et al.*, 2019]. As shown in Figure 1f, following the HTHH eruption there are more smaller particles with effective radii of 0.2-0.6 μm, consistent with the model runs from *Zhu et al.* [2022] and the estimations by *Khaykin et al.* [2022], which is indicative of increased sulfate aerosol concentrations.

3.2 Initial Evolution of HTHH Plume and Its Effect on MODIS SST

The early evolution and dispersion of the HTHH volcanic plume have been discussed [*Khaykin et al.*, 2022; *Legras et al.*, 2022; *Sellitto et al.*, 2022] using satellite observations. During the first

several hours after the eruption, the localized aerosol plume primarily consisted of aspherical particles, i.e., ash and/or ice crystals. Subsequently, a plume with large SO_2 content emerged to the west, meanwhile, the ash and ice components remained locally and dissipated gradually likely via sedimentation. On the following day, 16 January, an increase of spherical particles with low depolarization [*Legras et al.*, 2022; *Sellitto et al.*, 2022] was detected, suggesting the removal of ash/ice particles and fast formation of sulfate aerosols. Such rapid conversion of SO_2 to sulfate aerosols is at least two times faster than expected and has been explained as the presence of abundant H_2O in the plume injected into the stratosphere leading to the accelerated oxidation of SO_2 to H_2SO_4 [*Carn et al.*, 2022; *Zhu et al.*, 2022]. Therefore, we consider the enhancement of sulfate droplets as the predominant aerosol effect on the MODIS SST retrievals after the HTHH eruption.

Over the following weeks, the sulfate plume was quickly transported zonally by prevailing easterly winds in the stratosphere, as shown in Figure 2a-e, using the IMS SOD data. The extent of aerosol plume was largely consistent with strongly hydrated layers detected by the MLS, further indicating the fast formation of sulfate aerosols is due to H_2O abundance. To better reveal the impact of this advection on MODIS SST, four subregions are divided by longitude (I: 0º-90ºE; II: 90ºE-180ºE; III: 180ºW-90ºW; IV: 90ºW-0º). Additionally, the matchup SSTs are selected within the 30ºS-10ºS latitude band, and the statistics of ΔSST are shown as boxplots in Figure 2f. From Jan 16 to 20, 2022, the plume was mainly concentrated in region II with the head in region I (Figure 2a), as were the significantly negative biases in MODIS SST. Subsequently, the sulfate aerosols dominated in region I, leaving some residual effects in region II. Note that region IV was not obviously affected since most SST retrievals in the matchups were uncontaminated by the plume (Figure 2b). However, in the next few days, the aerosol effect was pronounced in region IV with a mean ΔSST of -0.66 K and a standard deviation of 0.72 K (Table S3 in Supporting Information S1), and was secondary in region III (Figure 2c). Actually, some the patches of plume were observed again in northern Australia at the end of January, showing a complete circumnavigation in two weeks. In early February, a feature of the plume, referred to as dragon-shaped by *Khaykin et al.* [2022], appeared with a head north of 10°S and a stronger tail at ~20°S extending across the Pacific (Figure 2d). By mid-February, abnormally negative ΔSSTs recurred in regions I and II, and the leading edge of the plume near 5°S caught up with the slowest at 25°S, covering all longitudes (Figure 2e). Overall, the evolution of negative MODIS SST anomalies are in good agreements with the footprints of sulfate aerosol plume in the month following the HTHH eruption.

3.3 Long-Term Variation of Volcanic Aerosol Effect on MODIS SST

With time, the volcanic aerosol plume continued elongating and dispersed over the whole Southern Hemisphere (SH) tropics, and was subsequently transported poleward by the Brewer–Dobson circulation (BDC) in weeks to months [*Khaykin et al.*, 2022]. As shown in Figure 3a, the stratospheric aerosol plume was transported within the barrier of the tropical pipe [*Plumb*, 1996]

from January to May. The poleward transport of the aerosol increased in June when the BDC in the tropics is enhanced during the SH winter, with a second core of extreme sAOD extending beyond 40°S. Figure 3b-c depicts the variation of monthly MODIS SST anomalies (defined as the difference between median ΔSST after the eruption compared to that of previous five years, i.e., 2017-2021) in two latitude bands, showing significant negative correlations with sAOD anomalies (defined as the zonal average of 2022-2021 sAOD difference). For 20°S-0°, the aerosol effect on SST reached a maximum in March, whereas it was insignificant initially and more pronounced later at 40°S-20°S. Note that the correlation coefficient between SST and sAOD anomalies for 40°S-20°S is only 0.66, much lower than that for 20°S-0° (0.91). This might be explained as the larger sampling errors caused by clouds in MODIS SST at mid-latitudes [*Liu and Minnett*, 2016]. Figure 3d-e provides the temporal evolution of OMPS-LP AMER field, and the major enhancements of aerosol concentration center on mid-stratosphere with some anomalies extending down to the tropopause. The aerosol layer is descending due to gravitational settling, more pronounced at 40°S-20°S, separating from the bulk of H_2O gradually rising with the diabatic circulation [*Schoeberl et al.*, 2022].

To quantify the aerosol-induced error in MODIS SST, RTTOV v13.1 atmospheric radiative transfer model [*Hocking et al.*, 2021] was used. The 2021 MUDB was matched with the meteorological fields from the MERRA-2 reanalysis as model inputs. As the majority of stratospheric aerosols is sulphated droplets, the Optical Properties of Aerosols and Clouds (OPAC; [*Hess et al.*, 1998]) pre-defined corresponding type (SUSO) is used in the simulations. The climatological aerosol profiles generated by the OPAC model are considered as the background aerosol, while the perturbations due to HTHH eruption are evaluated by the monthly mean ratio of 2022/2021 AMER, shown as vertical Gaussian-like distributions in Figure 3f-g. Table 2a displays the results for two months, February and August, in both latitude bands. The RTTOV-simulated MODIS SST anomalies (mean difference between SST with and without aerosol enhancement) due to HTHH volcanic sulfate aerosols generally have good agreements with those from the satellite retrievals. The model overestimations could be due to an exaggerated assessment of the growth rate of aerosol concentration, as in the MUDB the cloud-screening algorithm removes most pixels with high aerosol-contamination. Note that RTTOV simulates the background aerosol as introducing -0.03 K of mean SST anomaly, which is much smaller than the peak HTHH aerosol effect.

4 Discussion

This paper shows the negative biases of MODIS SST caused by the HTHH eruption are closely related to the sulfate aerosol from the volcanic plume, which was mainly concentrated in the mid-stratosphere. This aerosol effect lasted at least till the end of 2022 and would persist for some time into the future due to the several years' residence of stratospheric aerosols. The SST anomalies were pronounced following the eruption, while the peak appears in winter for southern mid-latitudes due to the BDC. Numerical simulation results from RTTOV are comparable to the magnitudes of the SST anomalies from MUDB, further demonstrating the dominant sulfate aerosol effect on MODIS SST.

Theoretically, aerosol-contaminated IR satellite SST retrievals are biased low because the aerosol absorbs the IR emission from surface and then emits at lower temperatures [*Walton*, 1985]. The current atmospheric correction algorithm mainly compensates for the radiance attenuation by H_2O, without accounting for the spectral absorptions by stratospheric aerosols connected with volcanic eruptions. Table 2b shows the RTTOV simulations for the BT deficits induced by sulfate aerosol and non-aerosol (mostly H_2O) components in the MODIS 11 μm and 12 μm bands after the HTHH eruption. Significantly, the BT deficit due to H_2O absorption at 12 μm is greater than that at 11μm, whereas the aerosol-induced attenuation is opposite. Such characteristics lead to under-compensations for the retrieved SST not only from the aerosol-induced BT deficit at 11 μm, but also from a small negative offset of BT difference (11-12 μm) by aerosols. The negative offsets of BT difference, -0.06 K on average, are observed in the MUDB (Figure S1a in Supporting Information S1). Although it has been reported the H_2O injection by HTHH into stratosphere is unprecedented in magnitude in the satellite era, the total column H_2O in the atmosphere tends to be reduced (Figure S1b in Supporting Information S1), indicating the effect of increased sulfate aerosol on the hydrological cycle as presented in the Mt. Pinatubo case [*Trenberth and Dai*, 2007]. Therefore, the reduction in BT difference might also be partially attributed to the total column H_2O reduction, which needs to be further investigated. Regardless, the algorithm coefficients should still be robust for the H_2O effect compensation since they always account best for the central part of the distribution (Figure S1b in Supporting Information S1).

Overall, although the magnitudes of the aerosol effects are much lower than those of H_2O, they introduce errors of several tenths Kelvin in SST retrieved through (1) in the SH. Furthermore, unlike the El Chichón and Mt. Pinatubo volcanic eruptions, HTHH did not cause anomalies in IR satellite-derived SST > 1 K. However, it is still necessary to develop a strategy or an improved algorithm to correct for the aerosol effects, considering the long duration and wide coverage with some parts of the plume crossing the equator, even extending towards the North Pole [*Khaykin et al.*, 2022].

Acknowledgement

We would like to specially thank Dr. Pedro Campuzano-Jost of the University of Colorado Boulder for providing information about aerosol chemistry.

Open Research

The MUDB for MODIS on Aqua is available from: https://seabass.gsfc.nasa.gov/archive/SSTVAL/2019.

MODIS on Aqua Level 2 AOD data files are available from: https://doi.org/10.5067/MODIS/MYD04_L2.061.

IMS sulphate-specific AOD can be accessed from: https://doi.org/10.5281/zenodo.7102472.

OMPS-LP v2.1 data are available from: https://doi.org/10.5067/CX2B9NW6FI27.

Aura MLS v4 H_2O data are available from: https://doi.org/10.5067/Aura/MLS/DATA2009.

MERRA-2 reanalysis data for the surface and vertical profiles of meteorological fields are available from: https://doi.org/10.5067/VJAFPLI1CSIV and https://doi.org/10.5067/SUOQESM06LPK respectively.

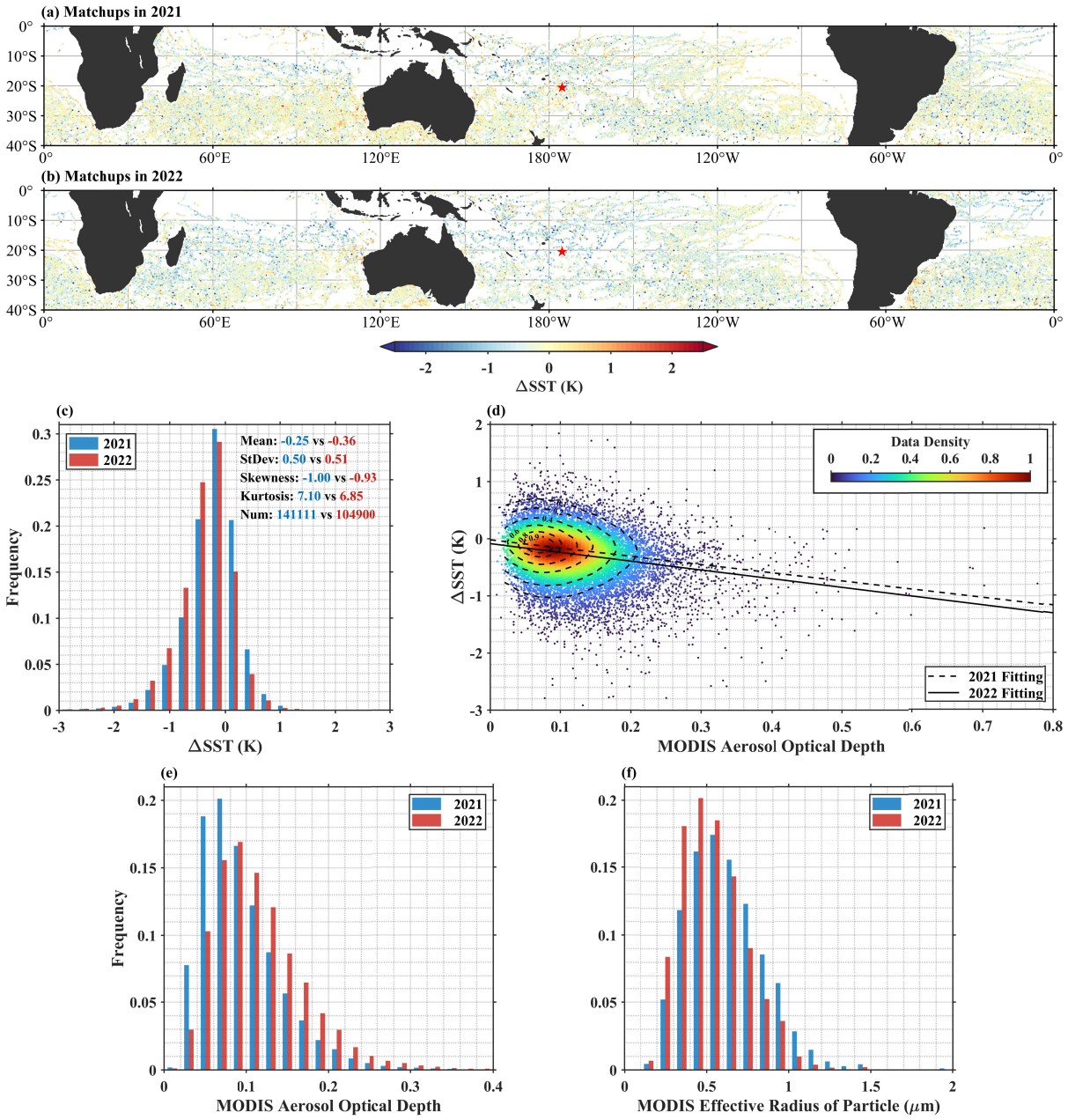

Fig. 1. Distribution of MODIS Aqua ΔSST (K) in (a) 2021 and (b) 2022. The red star indicates the location of the HTHH eruptions on 15 January, 2022. (c) Histogram of ΔSST annotated with statistics. (d) ΔSST as a function of MODIS daytime AOD at 550 nm in 2022, colored by the data density. The dashed contours are the data density in 2021. The dashed and solid lines are the fitted regressions for 2021 and 2022 respectively. (e) Histogram of MODIS AOD. (f) Histogram of MODIS effective radius (μm) of aerosol particles.

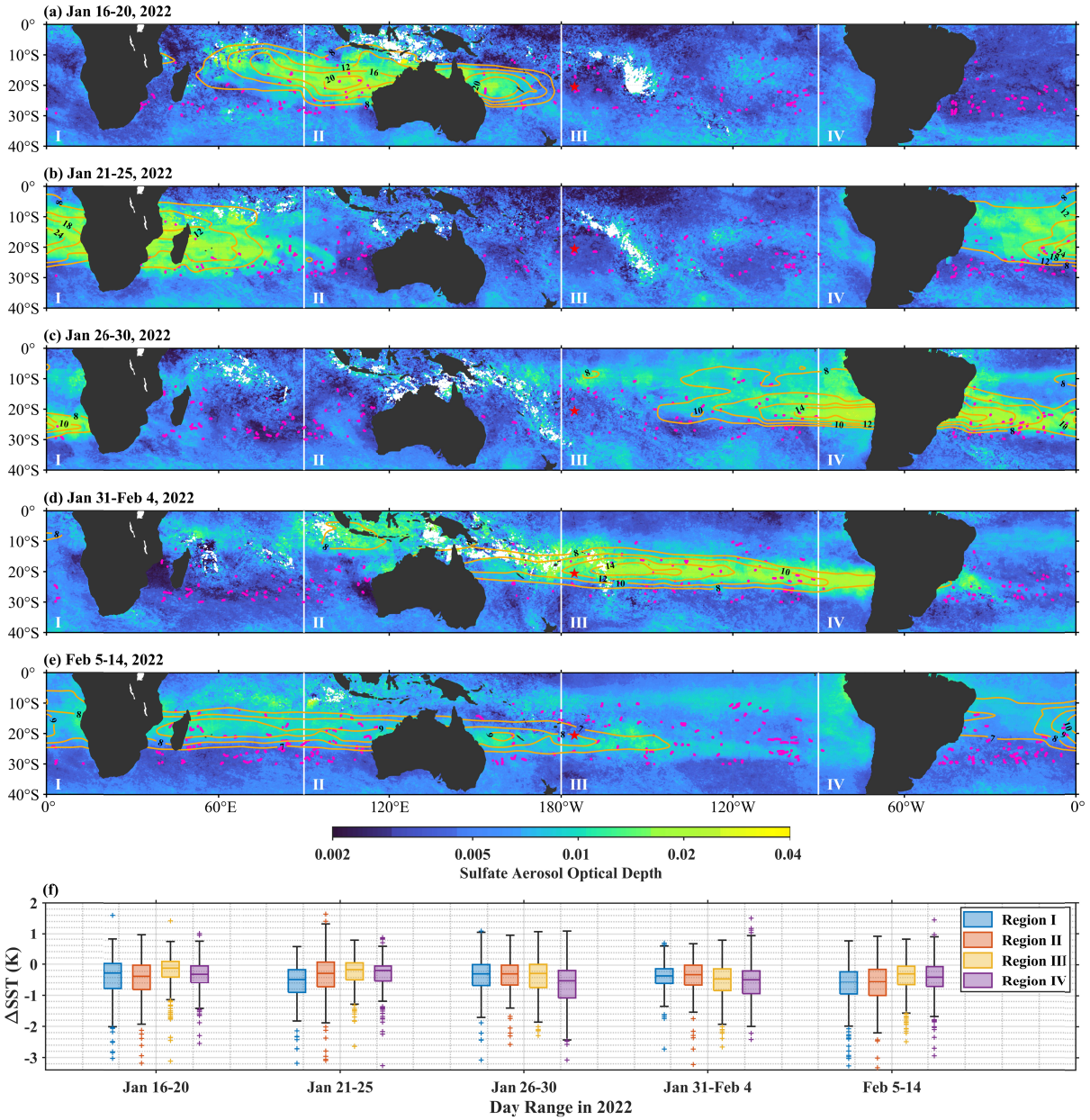

Fig. 2. Circumnavigation of the sulfate aerosol plume in the first 30 days after the HTHH eruption (red star), plotted from (a)-(e) as the mean IMS SOD (color; white patches are missing values) with MLS stratospheric mean (1-100 hPa) H_2O (tangerine contours; ppmv) in five successive time intervals. The zonal band is equally divided into four subregions by longitude starting from 0º. The locations of SST matchups between 30ºS and 10ºS in each interval are given by magenta dots. (f) Boxplots of ΔSST for each subregion in interval. The plus signs indicate outliers.

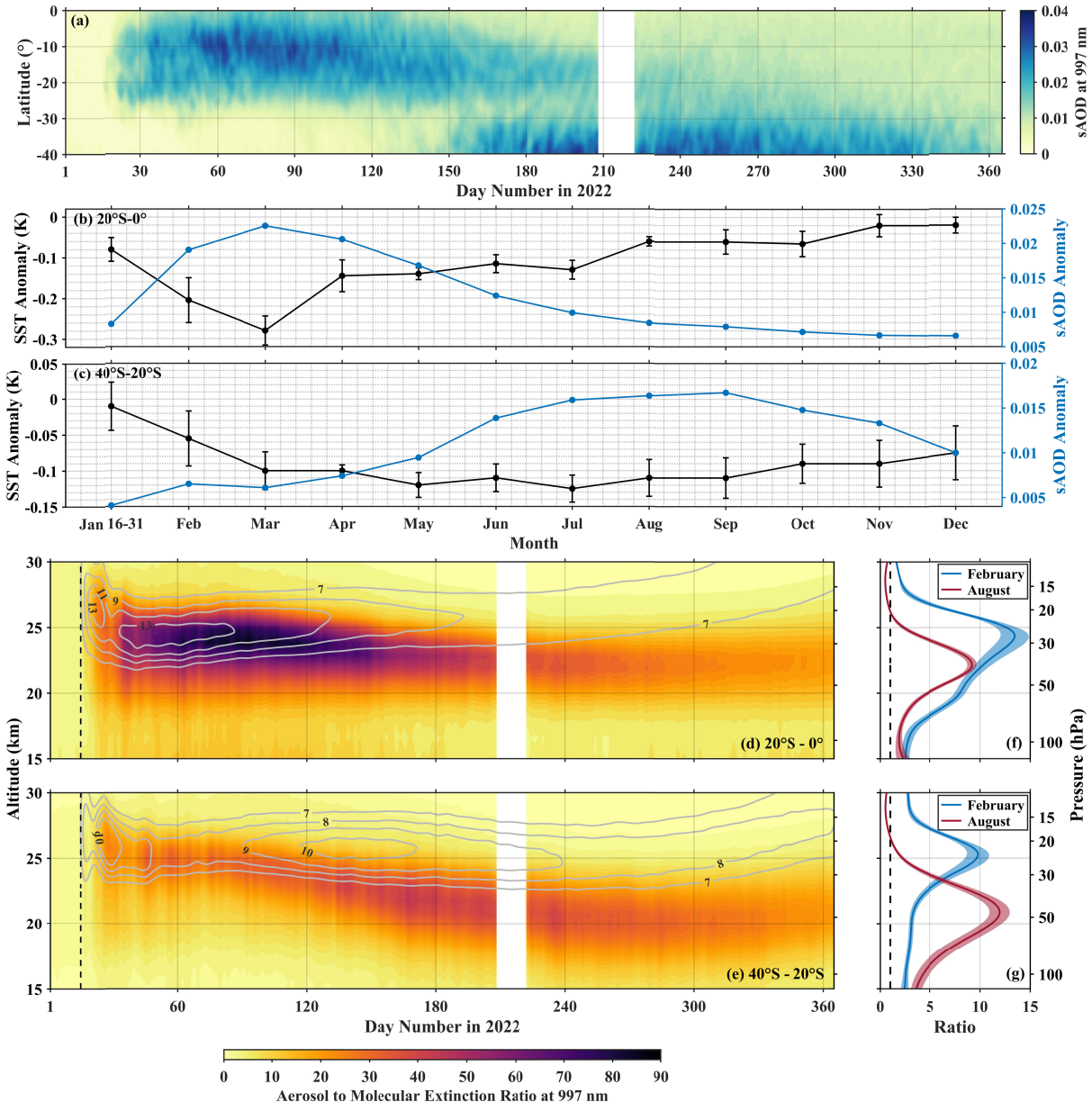

Fig. 3. (a) Time series of OMPS-LP sAOD at 997 nm zonally averaged in 2022. (b) Monthly variation of MODIS SST anomaly (black) and OMPS-LP sAOD anomaly (blue) within 20ºS-0º latitude band. The error bars indicate the variations of monthly ΔSST medians from 2017 to 2021. (c) As (b), but for 40ºS-20ºS. (d) Time series of the OMPS-LP AMER (color) and MLS H_2O (contour) zonal mean profile between 20ºS and 0º. (e) As (d), but for 40ºS-20ºS. (f) Monthly mean (line) ±1 standard deviation (envelope) of the ratio of OMPS-LP AMER in 2022 and 2021 for February (blue) and August (red) for 20ºS-0º. (g) As (f), but for 40ºS-20ºS.

Table 1. Statistics of MODIS Aqua ΔSST (K) between 40ºS-0º and 180ºW-180ºE, including the mean, median, standard deviation, robust standard deviation and number of data, are presented in terms of (a) day and night flags and (b) quality flags.

(a)	**Day**		**Night**		**Total**	
	2021	2022	2021	2022	2021	2022
Mean	-0.231	-0.342	-0.272	-0.388	-0.250	-0.363
Median	-0.175	-0.285	-0.210	-0.320	-0.195	-0.300
StDev	0.492	0.494	0.509	0.508	0.500	0.501
Robust StDev	0.419	0.426	0.381	0.393	0.400	0.411
Number	76056	56262	65055	48638	141111	104900

(b)	**QL = 0**		**QL = 1**		**Total**	
	2021	2022	2021	2022	2021	2022
Mean	-0.204	-0.305	-0.340	-0.474	-0.250	-0.363
Median	-0.160	-0.260	-0.290	-0.420	-0.195	-0.300
StDev	0.431	0.433	0.603	0.595	0.500	0.501
Robust StDev	0.344	0.344	0.533	0.541	0.400	0.411
Number	93533	68648	47578	36252	141111	104900

Table 2. RTTOV simulations of (a) the mean negative biases (K) of MODIS-retrieved SST caused by HTHH volcanic sulfate aerosol compared with the results from matchup data and (b) the mean BT deficits (K) in 11 μm and 12 μm channels with the corresponding BT difference induced by aerosol and H_2O.

(a)	**February**			**August**		
	MUDB	RTTOV	Number	MUDB	RTTOV	Number
20ºS-0º	-0.205	-0.242	2596	-0.060	-0.089	2722
40ºS -20ºS	-0.055	-0.091	9956	-0.110	-0.144	8699

(b)		**February**			**August**		
		BT_{11} Deficit	BT_{12} Deficit	BT_{11}-BT_{12}	BT_{11} Deficit	BT_{12} Deficit	BT_{11}-BT_{12}
20ºS-0ºS	Aerosol	-0.228	-0.174	-0.054	-0.097	-0.079	-0.018
	H_2O	-6.970	-8.330	1.361	-5.870	-6.947	1.077
40ºS-20ºS	Aerosol	-0.085	-0.065	-0.020	-0.105	-0.064	-0.041
	H_2O	-5.423	-6.490	1.067	-3.761	-4.558	0.797

References

Carn, S. A., N. A. Krotkov, B. L. Fisher, and C. Li (2022), Out of the blue: Volcanic SO2 emissions during the 2021–2022 eruptions of Hunga Tonga—Hunga Ha'apai (Tonga), *Frontiers in Earth Science*, *10*.

Donlon, C. J., P. J. Minnett, C. Gentemann, T. J. Nightingale, I. J. Barton, B. Ward, and M. J. Murray (2002), Toward improved validation of satellite sea surface skin temperature measurements for climate research, *Journal of Climate*, *15*(4), 353-369.

Gelaro, R., et al. (2017), The Modern-Era Retrospective Analysis for Research and Applications, Version 2 (MERRA-2), *Journal of Climate*, *30*(14), 5419-5454.

Guo, S., G. J. S. Bluth, W. I. Rose, I. M. Watson, and A. J. Prata (2004), Re-evaluation of SO2 release of the 15 June 1991 Pinatubo eruption using ultraviolet and infrared satellite sensors, *Geochemistry, Geophysics, Geosystems*, *5*(4).

Hess, M., P. Koepke, and I. Schult (1998), Optical Properties of Aerosols and Clouds: The Software Package OPAC, *Bulletin of the American Meteorological Society*, *79*(5), 831-844.

Hocking, J., J. Vidot, P. Brunel, P. Roquet, B. Silveira, E. Turner, and C. Lupu (2021), A new gas absorption optical depth parameterisation for RTTOV version 13, *Geosci. Model Dev.*, *14*(5), 2899-2915.

Jenkins, S., C. Smith, M. Allen, and R. Grainger (2023), Tonga eruption increases chance of temporary surface temperature anomaly above 1.5 °C, *Nature Climate Change*, *13*(2), 127-129.

Jia, C., and P. J. Minnett (2020), High latitude sea surface temperatures derived from MODIS infrared measurements, *Remote Sensing of Environment*, *251*, 112094.

Khaykin, S., et al. (2022), Global perturbation of stratospheric water and aerosol burden by Hunga eruption, *Communications Earth & Environment*, *3*(1), 316.

Kilpatrick, K. A., G. Podestá, E. Williams, S. Walsh, and P. J. Minnett (2019), Alternating Decision Trees for Cloud Masking in MODIS and VIIRS NASA Sea Surface Temperature Products, *Journal of Atmospheric and Oceanic Technology*, *36*(3), 387-407.

Kilpatrick, K. A., G. Podestá, S. Walsh, E. Williams, V. Halliwell, M. Szczodrak, O. B. Brown, P. J. Minnett, and R. Evans (2015), A decade of sea surface temperature from MODIS, *Remote Sensing of Environment*, *165*, 27-41.

Legras, B., C. Duchamp, P. Sellitto, A. Podglajen, E. Carboni, R. Siddans, J. U. Grooß, S. Khaykin, and F. Ploeger (2022), The evolution and dynamics of the Hunga Tonga–Hunga Ha'apai sulfate aerosol plume in the stratosphere, *Atmos. Chem. Phys.*, *22*(22), 14957-14970.

Levy, R. C., S. Mattoo, L. A. Munchak, L. A. Remer, A. M. Sayer, F. Patadia, and N. C. Hsu (2013), The Collection 6 MODIS aerosol products over land and ocean, *Atmos. Meas. Tech.*, *6*(11), 2989-3034.

Liu, Y., and P. J. Minnett (2016), Sampling errors in satellite-derived infrared sea-surface temperatures. Part I: Global and regional MODIS fields, *Remote Sensing of Environment*, *177*, 48-64.

Livesey, N. J., W. V. Snyder, W. G. Read, and P. A. Wagner (2006), Retrieval algorithms for the EOS Microwave limb sounder (MLS), *IEEE Transactions on Geoscience and Remote Sensing*, *44*(5), 1144-1155.

Lumpkin, R., N. Maximenko, and M. Pazos (2012), Evaluating Where and Why Drifters Die, *Journal of Atmospheric and Oceanic Technology*, *29*(2), 300-308.

Luo, B., P. J. Minnett, C. Gentemann, and G. Szczodrak (2019), Improving satellite retrieved night-time infrared sea surface temperatures in aerosol contaminated regions, *Remote Sensing of Environment*, *223*, 8-20.

Millán, L., et al. (2022), The Hunga Tonga-Hunga Ha'apai Hydration of the Stratosphere, *Geophysical Research Letters*, *49*(13), e2022GL099381.

Minnett, P. J., K. Kilpatrick, G. Podestá, E. Williams, and S. Walsh (2016), Skin sea-surface temperatures from MODIS & VIIRS, *Poster presented at the 17th International GHRSST Science Team Meeting, Washington DC, USA*.

Minnett, P. J., et al. (2020), Skin Sea-Surface Temperature from VIIRS on Suomi-NPP—NASA Continuity Retrievals, *Remote Sensing*, *12*(20).

Plumb, R. A. (1996), A “tropical pipe” model of stratospheric transport, *Journal of Geophysical Research: Atmospheres*, *101*(D2), 3957-3972.

Read, W. G., L. Froidevaux, and J. W. Waters (1993), Microwave limb sounder measurement of stratospheric SO2 from the Mt. Pinatubo Volcano, *Geophysical Research Letters*, *20*(12), 1299-1302.

Remer, L. A., et al. (2005), The MODIS Aerosol Algorithm, Products, and Validation, *Journal of the Atmospheric Sciences*, *62*(4), 947-973.

Reynolds, R. W. (1993), Impact of Mount Pinatubo Aerosols on Satellite-derived Sea Surface Temperatures, *Journal of Climate*, *6*(4), 768-774.

Reynolds, R. W., C. K. Folland, and D. E. Parker (1989), Biases in satellite-derived sea-surface-temperature data, *Nature*, *341*(6244), 728-731.

Saunders, R., J. Hocking, D. Rundle, P. Rayer, S. Havemann, M. Matricardi, A. Geer, C. Lupu, P. Brunel, and J. Vidot (2017), RTTOV v12 science and validation report, 78.

Schoeberl, M. R., Y. Wang, R. Ueyama, G. Taha, E. Jensen, and W. Yu (2022), Analysis and Impact of the Hunga Tonga-Hunga Ha'apai Stratospheric Water Vapor Plume, *Geophysical Research Letters*, *49*(20), e2022GL100248.

Sellitto, P., and B. Legras (2016), Sensitivity of thermal infrared nadir instruments to the chemical and microphysical properties of UTLS secondary sulfate aerosols, *Atmos. Meas. Tech.*, *9*(1), 115-132.

Sellitto, P., et al. (2022), The unexpected radiative impact of the Hunga Tonga eruption of 15th January 2022, *Communications Earth & Environment*, *3*(1), 288.

Siddans, R. (2019), Water Vapour Climate Change Initiative (WV_cci) - Phase One, Deliverable 2.2; Version 1.0.*Rep.*, STFC Rutherford Appleton Laboratory (RAL).

Szczodrak, M., P. J. Minnett, and R. H. Evans (2014), The effects of anomalous atmospheres on the accuracy of infrared sea-surface temperature retrievals: Dry air layer intrusions over the tropical ocean, *Remote Sensing of Environment*, *140*, 450-465.

Taha, G., R. Loughman, T. Zhu, L. Thomason, J. Kar, L. Rieger, and A. Bourassa (2021), OMPS LP Version 2.0 multi-wavelength aerosol extinction coefficient retrieval algorithm, *Atmos. Meas. Tech.*, *14*(2), 1015-1036.

Trenberth, K. E., and A. Dai (2007), Effects of Mount Pinatubo volcanic eruption on the hydrological cycle as an analog of geoengineering, *Geophysical Research Letters*, *34*(15).

Walton, C. (1985), Satellite Measurement of Sea Surface Temperature in the Presence of Volcanic Aerosols, *Journal of Applied Meteorology and Climatology*, *24*(6), 501-507.

Walton, C. C., W. G. Pichel, J. F. Sapper, and D. A. May (1998), The development and operational application of nonlinear algorithms for the measurement of sea surface temperatures with the NOAA polar-orbiting environmental satellites, *Journal of Geophysical Research: Oceans*, *103*(C12), 27999-28012.

Zhu, Y., et al. (2022), Perturbations in stratospheric aerosol evolution due to the water-rich plume of the 2022 Hunga-Tonga eruption, *Communications Earth & Environment*, *3*(1), 248.